

Radiatively-driven clumpy X-ray absorbers in the NLS1 galaxy IRAS 13224–3809

TAKUYA MIDOOKA,^{1,2} MISAKI MIZUMOTO,³ AND KEN EBISAWA^{1,2}

¹*Institute of Space and Astronautical Science, Japan Aerospace Exploration Agency,
3-1-1 Yoshinodai, Chuo-ku, Sagami-hara, Kanagawa 252-5210, Japan*

²*Department of Astronomy, Graduate School of Science, The University of Tokyo
7-3-1 Hongo, Bunkyo-ku, Tokyo 113-8654 Japan*

³*Science education research unit, University of Teacher Education Fukuoka,
1-1 Akama-bunkyo-machi, Munakata, Fukuoka 811-4192, Japan*

(Received; Revised July 25, 2023; Accepted)

Submitted to ApJ

ABSTRACT

Recent radiation-magnetohydrodynamic simulations of active galactic nuclei predict the presence of the disk winds, which may get unstable and turn into fragmented clumps far from the central black hole. These inner winds and the outer clumps may be observed as the ultrafast outflows (UFOs) and the partial absorbers, respectively. However, it is challenging to observationally constrain their origins because of the complicated spectral features and variations. To resolve such degeneracies of the clumpy absorbers and other components, we developed a novel “spectral-ratio model fitting” technique that estimates the variable absorbing parameters from the ratios of the partially absorbed spectra to the non-absorbed one, canceling the complex non-variable spectral features. We applied this method to the narrow-line Seyfert 1 galaxy IRAS 13224–3809 observed by *XMM-Newton* in 2016 for ~ 1.5 Ms. As a result, we found that the soft spectral variation is mostly caused by changes in the partial covering fraction of the mildly-ionized clumpy absorbers, whose outflow velocities are similar to those of the UFO (~ 0.2 – $0.3 c$). Furthermore, the velocities of the clumpy absorbers and UFOs increase similarly with the X-ray fluxes, consistent with the change in the UV-dominant continuum flux. We also discovered a striking correlation between the clump covering fraction and the equivalent width of the UFO absorption lines, which indicates that increasing the outflow in the line-of-sight lead to more prominent UFOs and more partial absorption. These findings strongly suggest that the clumpy absorbers and the UFO share the same origin, driven by the same UV-dominant continuum radiation.

Keywords: Active galactic nuclei (16) — Seyfert galaxies (1447) — X-ray astronomy(1810)

1. INTRODUCTION

Active galactic nuclei (AGNs) are powered by accretion onto supermassive black holes (SMBHs). Recent observational and theoretical studies suggest that most AGNs have multiple ionized absorbers (see review by e.g., Laha et al. 2021). Broadly speaking, three types of absorbers have been proposed. The first one is the *warm absorbers* (WAs), which are detected as absorption lines

and edges in the soft X-ray band of $\sim 65\%$ of the nearby AGNs, especially in the radio-quiet Seyfert 1 galaxies (e.g., McKernan et al. 2007, Laha et al. 2014). These absorbers are known to be mildly ionized and blue-shifted with a velocity of $\lesssim 2000$ km/s.

The second one is the *partial covering absorbers*, which partially absorb the X-ray continuum in the line of sight. This is also called the “obscurer”, which causes simultaneous soft X-ray and UV absorption troughs (e.g., NGC 5548; Kaastra et al. 2014).

The third one is the *ultrafast outflow* (UFO). Seyfert galaxies often have blue-shifted, highly ionized iron K-absorption lines in their 30–40% of the X-ray spectra

Corresponding author: Takuya Midooka, Misaki Mizumoto
midooka@ac.jaxa.jp, mizumoto-m@fukuoka-edu.ac.jp

(Tombesi et al. 2010; Gofford et al. 2013; Igo et al. 2020; Matzeu et al. 2023). The UFOs are considered to be the outflowing winds from the accretion disk at very high velocities of 0.1–0.3 c , where c is the speed of light. Since UFOs are likely to have larger solid angles than the relativistic jets (e.g., Nardini et al. 2015, Hagino et al. 2015), UFO contribution to the co-evolution of the SMBHs and the host galaxies may be comparable to or even exceed that of the jets (e.g., King 2010, King & Pounds 2015).

IRAS 13224–3809 is a narrow-line Seyfert 1 (NLS1) galaxy with a SMBH of about $10^{6-7} M_{\odot}$ at $z = 0.0658$ (e.g., Emmanoulopoulos et al. 2014; Chiang et al. 2015; Alston et al. 2019), accreting close to or above the Eddington limit (Alston et al. 2019). In this object, Parker et al. (2017) discovered UFO absorption lines in the 1.5 Ms deep observation by *XMM-Newton* in 2016. They claimed that the equivalent width of the UFO absorption lines and the X-ray luminosity are anti-correlated, while the line-of-sight velocity of the UFO is correlated with the X-ray luminosity.

Some previous studies including Parker et al. (2017) explained the X-ray spectra of IRAS 13224–3809 in terms of the relativistic disk reflection model (e.g., Fabian et al. 1989), which assumes such extreme physical conditions that the central black hole spin is almost maximum and the most incident X-ray radiation from a tiny source is reflected at the innermost region of the disk (e.g., Fabian et al. 2009). This model also requires an iron overabundance by a factor of 3–20 to account for energy spectra of various objects (e.g., Fabian et al. 2013, Chiang et al. 2015). In a recent study, Jiang et al. (2022) reported that the iron abundance Z_{Fe} is 3.2 ± 0.5 when assuming a high-density disk reflection of 10^{20} cm^{-3} . In the X-ray spectra of AGN, the relativistic reflection model and the partial absorption model are often indistinguishable in shape (e.g., Parker et al. 2022). In fact, Yamasaki et al. (2016) successfully explained the spectral variability of IRAS 13224–3809 (*XMM-Newton* data in 2001–2011 before detection of the UFO absorption) using the partial absorption model without such extreme conditions.

Two-dimensional radiation-magnetohydrodynamic simulations of supercritical accretion flows show that the radiation pressure generates disk winds, which become clumpy at a few hundred Schwarzschild radius (R_{s}) (Takeuchi et al. 2013). They argued that the clump formation is probably because the Rayleigh-Taylor instability works efficiently where the radiation pressure is dominant over the gravitational potential. In addition to the Rayleigh-Taylor instability, contribution of the radiation hydrodynamic instability to the clump forma-

tion is also suggested in two- or three-dimensional radiation hydrodynamic simulations (e.g., Takeuchi et al. 2014, Kobayashi et al. 2018). Another mechanism has been proposed for the disk wind to get clumpy: Dannen et al. (2020) found through a parsec-scale wind simulation that dynamical thermal instability occurs in some zones, causing fragmentation of the outflow beyond the acceleration radius of the wind.

Mizumoto et al. (2019) proposed the “hot inner and clumpy outer wind model”, in which the inner wind and outer clumps may actually be observed as the UFOs and the clumpy absorbers, respectively. However, in the standard X-ray spectral analysis, parameters of the clumpy absorbers and other components such as WAs are often degenerate and difficult to be disentangled.

Recently, we developed a new data analysis technique called “spectral-ratio model fitting” to disentangle the spectral parameter degeneracy (Midooka et al. 2022b, hereafter Paper 1). In this method, by taking the spectral ratios of the intensity-sliced spectra, spectral variations only due to change of the partial absorbers are manifested, canceling out the invariable continuum and absorption features.

In this paper, we aim to constrain the outflowing velocity of the clumpy absorbers of IRAS 13224–3809 using the spectral ratio fitting method, and search for a plausible origin of the outflow and clumps.

2. OBSERVATIONS AND METHODS

2.1. Observations and Data reduction

We used the 1.5 Ms data obtained by *XMM-Newton* EPIC-pn (Jansen et al. 2001, Strüder et al. 2001) and OM (Mason et al. 2001) in the summer of 2016, including the unscheduled observations (see Table 1 in Paper 1). As our study requires a consecutive dataset taken within a short period of time, we did not incorporate any archival data before 2016. In addition to the pn, of which data processing was described in Paper 1, the OM data taken with the UVW1 filter is reduced with the standard SAS routine `omchain`, and the spectrum is extracted using `om2pha`.

Since the UFO properties of IRAS 13224–3809 are known to be luminosity-dependent (e.g., Parker et al. 2017, Pinto et al. 2018, and Chartas & Canas 2018), we created the intensity-sliced spectra. First, all the 0.3–10.0 keV events were binned into 1 ks intervals, as in previous studies (Parker et al. 2017; Pinto et al. 2018). We grouped the data into 10 intensity levels based on the flux in the 0.3–10 keV range and generated 10 intensity-sliced spectra (see Table 2 in Paper 1), which are labeled from A (the brightest) to J (the dimmest). The sliced spectral bins are grouped with 8 and 16 bins in 0.3–

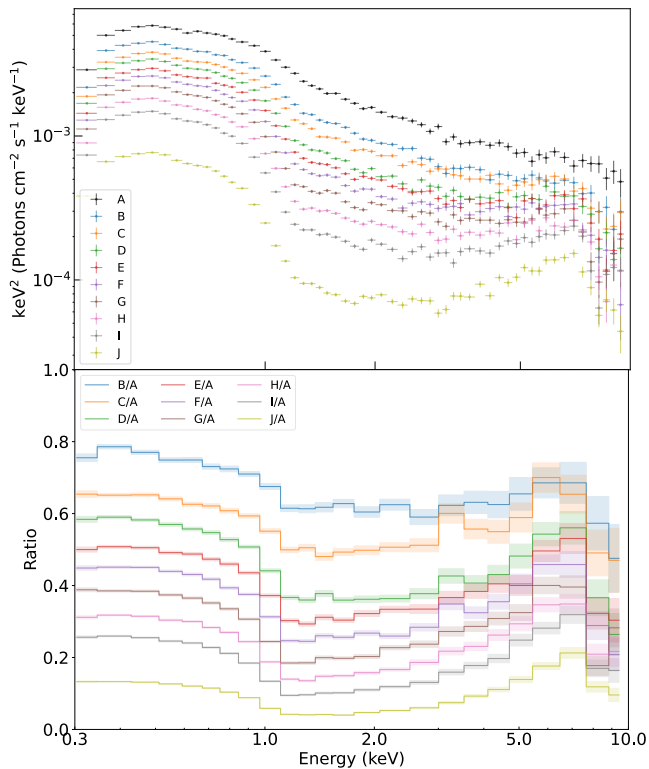


Figure 1. Top panel shows the 10 intensity-sliced spectra obtained by *XMM-Newton* pn in 0.3–10.0 keV. The νF_ν plot unfolded by the power-law with the index of 2.0 is shown. The bottom panel shows the nine spectral ratios to the brightest spectrum A (black in the top panel). Note that both panels show adequately binned spectra to enhance visibility.

2.0 keV and 2.0–10.0 keV, respectively. These intensity-sliced spectra are shown in the upper panel of Figure 1. Next, the observed spectral ratios are created by taking the ratio of each intensity-sliced spectrum (B–J) to the brightest spectrum A (lower panel of Figure 1).

2.2. Method of the spectral-ratio model fitting

We briefly describe the spectral-ratio model fitting method, details of which were explained in Paper 1. The spectral continuum of IRAS 13224–3809 consists of the power-law (PL) and the soft-excess component, and the continuum is absorbed by several intervening gases such as WA, UFO, and clumpy absorbers. WAs do not change their geometry or ionization structure significantly in a timescale of a few weeks, while the partial covering fraction of the clumpy absorbers, whose variation influences the spectral shape below ~ 5 keV, significantly changes in this timescale (e.g., Di Gesu et al. 2015, Midooka et al. 2022a). Therefore, taking the spectral ratio below 5 keV enables us to focus on the variability of the clumpy absorbers, canceling out the less time-variable spectral components. It should be noted that a similar

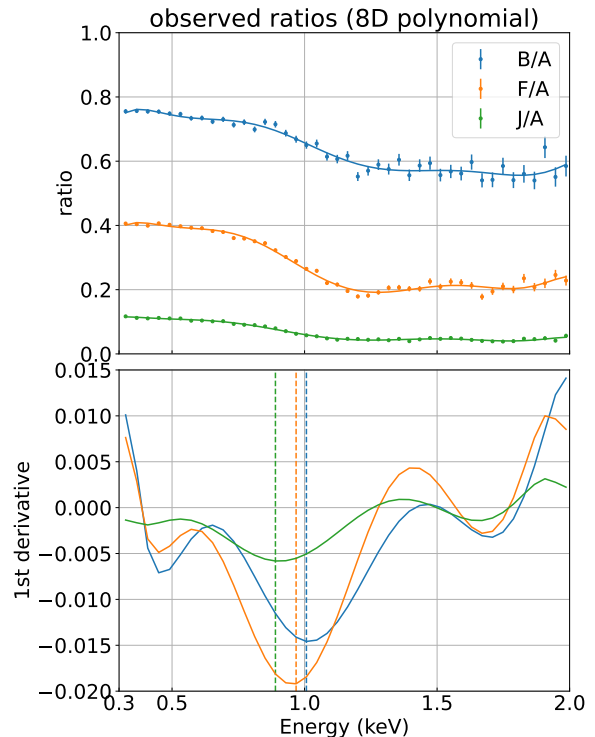


Figure 2. In the upper panel, scattered points show the observed spectral ratios B/A, F/A, and J/A. Solid lines are the best-fit 8th-order polynomial equations. The lower panel shows their 1st derivatives, in which the dotted vertical lines represent the energies where the 1st derivatives get minimum. These energies, characterizing the dip feature, increases as the X-ray flux gets higher.

spectral-ratio technique has been successfully adopted to study variation of the high energy cutoff in the AGN spectra (Zhang et al. 2018).

Model spectral ratios in 0.3–5.0 keV are calculated using XSPEC (version 12.12.0). We consider a simple model spectrum in which the continuum is covered by an ionized partial absorber (*zxcpcf*; Reeves et al. 2008). This absorber model has three parameters; ionization parameter ξ , hydrogen column density N_H , and partial covering fraction (CF). A table model of the spectral ratio is created by taking the ratio of the absorbed model spectra to the non-absorbed one (CF=0) with the same continuum parameters (see Figure 2 in Paper 1).

The three parameters of the clumpy absorber determine the shape of the spectral ratio, including the characteristic dip structures in 0.8–1.0 keV (Figure 2 in Paper 1). Fitting the observed and model spectral ratios makes it possible to constrain the partial absorber parameters without being affected by complicated WA spectral features.

3. DATA ANALYSIS AND RESULTS

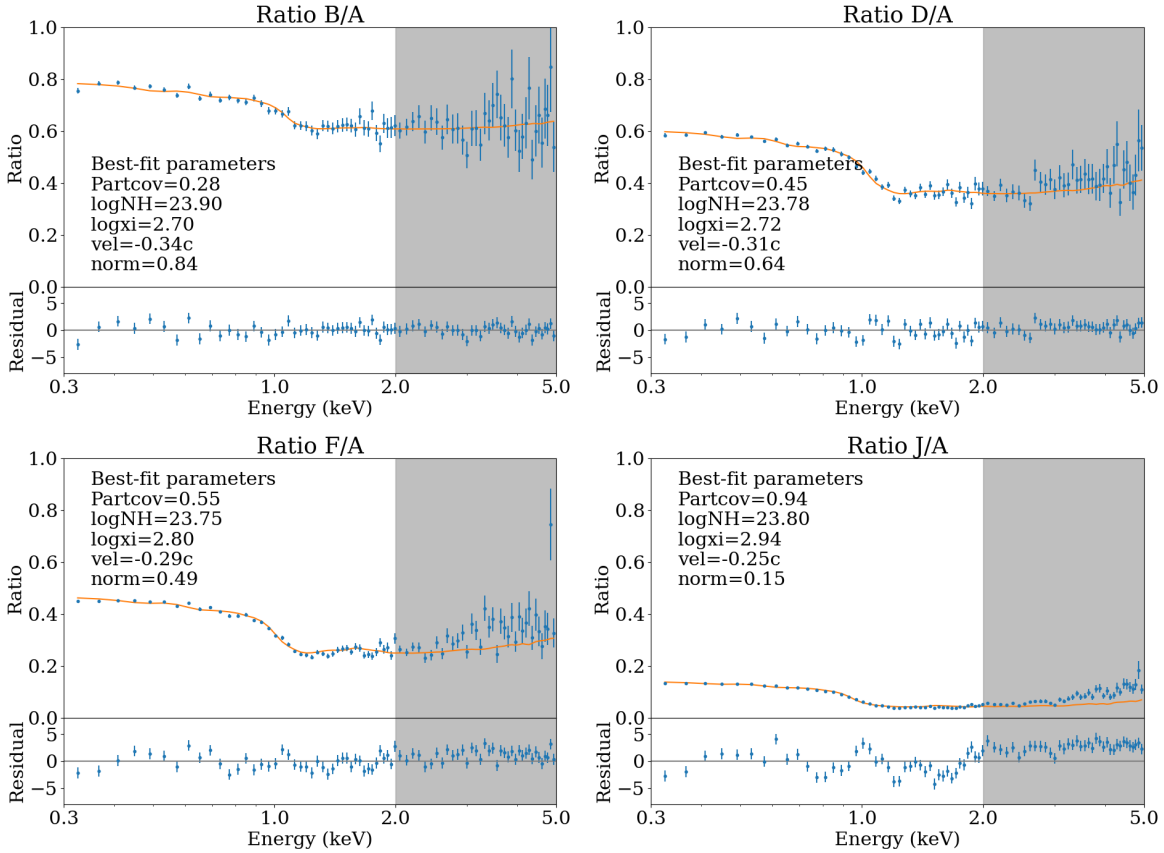


Figure 3. Examples of the spectral-ratio model fitting with the least chi-square method (B/A, D/A, F/A, and J/A). Fitting for the dimmer ones shows more significant residuals above ~ 2 keV, suggesting changes in the PL index, which is not taken into account here. The absorber parameters are constrained by the fitting below 2 keV, so the energy bands above 2 keV are shaded in gray.

3.1. Model-independent study of the spectral ratios

One of the purposes of the present study is to constrain the clump outflow velocities. In this section, we show that the flux dependency of the clump velocity can be constrained model-independently from the spectral ratios.

We made 9 spectral ratios from the 10 observed intensity-sliced spectra. The upper panel in Figure 2 shows the representative spectral ratios of B/A, F/A, and J/A, each of which has a dip- or cliff-like structure at around 1 keV. We define the “dip characteristic energy” where the spectral ratio changes from convex-upward to convex-downward. To do so, first, the observed spectral ratios are fitted with 8th-order polynomial equations (solid lines in the upper-panel in Figure 2). Then, the first derivatives of the 8th-order equation models are calculated (lower panel in Figure 2). The energies that give the minimums of the first derivative correspond to the dip characteristic energies defined above (dotted vertical lines in the lower panel of Figure 2). We find that the dip characteristic energy is *blue-shifted* when X-rays

get brighter. Note that this result is obtained without assuming any spectral models.

We note that the relativistic reflection model (e.g., Parker et al. 2017, Pinto et al. 2018, Chartas & Canas 2018, and Jiang et al. 2022) can also reproduce these spectral ratios, because the individual spectra are fitted. However, changes in the continuum and/or disk reflection normalizations are insufficient to account for the observed blue-shift of the dip structure, and the disk geometry and other parameters need to change concordantly to realize such spectral changes. We do not discuss this possibility any further in this paper.

3.2. Spectral-ratio model fitting in 0.3–5 keV

Next, we are going to fit the observed spectral ratios with physical models to constrain absorbers’ parameters. Having noticed the blue-shifted absorption features around 1 keV, we introduce the clumpy absorber velocity v_{out} in addition to the three clump parameters (CF, N_{H} , and ξ). Also, the continuum normalization ratio is a free parameter.

Table 1. Best-fit parameters obtained from spectral ratio model fitting with the least chi-squared (upper) and the MCMC estimation (lower). Note that N_{H} and ξ are tied in the least chi-square fitting, and only N_{H} is tied in the MCMC for all the spectral ratios.

Chi-sq	J	I	H	G	F	E	D	C	B
CF	0.86	0.78	0.70	0.65	0.58	0.53	0.51	0.32	0.28
norm	0.15	0.29	0.35	0.43	0.50	0.55	0.63	0.68	0.80
$\log N_{\text{H}}$ (tied)	23.8	23.8	23.8	23.8	23.8	23.8	23.8	23.8	23.8
$\log \xi$ (tied)	2.87	2.87	2.87	2.87	2.87	2.87	2.87	2.87	2.87
velocity (/c)	0.26	0.27	0.28	0.28	0.29	0.31	0.31	0.31	0.32

MCMC	J	I	H	G	F	E	D	C	B
CF	0.88	0.93	0.67	0.62	0.61	0.48	0.51	0.40	0.26
norm	0.15	0.29	0.36	0.43	0.50	0.55	0.63	0.68	0.80
$\log N_{\text{H}}$ (tied)	23.8	23.8	23.8	23.8	23.8	23.8	23.8	23.8	23.8
$\log \xi$	2.89	3.01	2.84	2.84	2.91	2.79	2.88	3.02	2.79
velocity (/c)	0.25	0.25	0.27	0.28	0.29	0.31	0.31	0.30	0.31

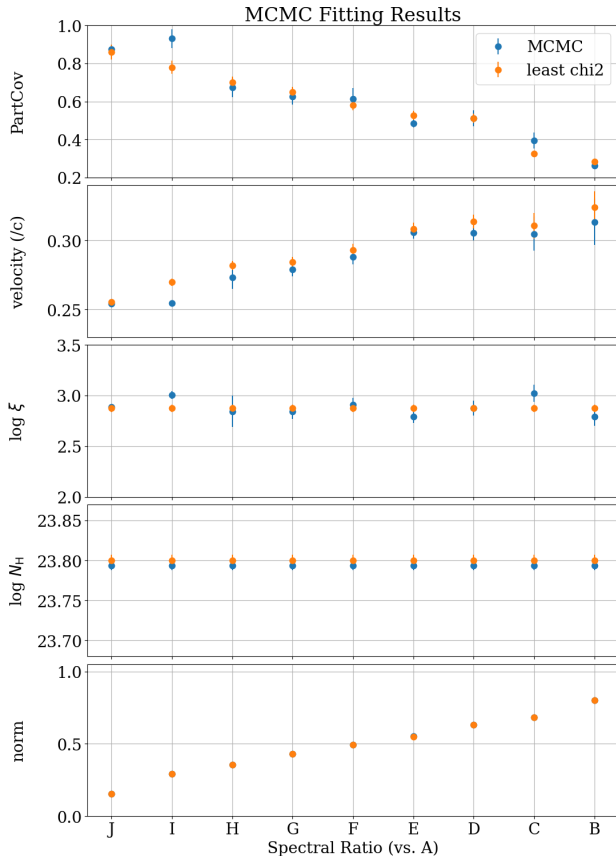


Figure 4. Best-fit parameters determined by the simultaneous least chi-square fitting (in orange) and MCMC estimation (in blue) to the nine intensity-sliced spectral ratios. N_{H} and ξ are tied in the least chi-square fitting, and only N_{H} is tied in the MCMC for all the spectral ratios. These parameters are indicated in Table 1.

Spectral-ratio table model was created with these four free parameters (CF, ξ , N_{H} , and v_{out} ; see Table 3 in Paper 1), where models are linearly interpolated between the adjacent grid points using the XSPEC built-in function. First, the least-square fitting was performed for the nine observed spectral ratios allowing all the five parameters free (the four parameters above and the normalization). We found that the N_{H} and ξ were not significantly variable among the nine ratios ($2.7 < \log \xi < 3.0$, $23.7 < \log N_{\text{H}} < 23.9$). Thus we tied these two parameters for all the nine spectral ratios and performed simultaneous fitting.

Table 1 shows all the fitting results, and Figure 3 shows examples of the fitting B/A, D/A, F/A, and J/A. The fitting was successful in all the spectral ratios below ~ 2 keV, where the absorbers’ parameters are constrained. Note that the model does not fit well above ~ 3 keV, especially in dimmer spectral ratios, suggesting a change in the photon index, that is confirmed later in the spectral fitting (section 3.3). The best-fit parameters are illustrated in Figure 4. We found that the partial covering fraction is smaller and the norm is higher as the X-ray flux gets higher. The outflow velocity of the partial absorber was 0.2–0.3 c , unexpectedly fast, even comparable to that of the UFOs reported in previous studies (Parker et al. 2017; Pinto et al. 2018; Chartas & Canas 2018). Furthermore, the velocity was found to be higher when the X-ray flux is higher.

We aim to confirm that the velocity we have obtained is determined independently, not being degenerate with the ionization parameter ξ , since both parameters similarly affect absorption line/edge energies. We perform a Markov Chain Monte Carlo (MCMC) calculation using the “emcee” package (Foreman-Mackey et al. 2013) to

determine the posterior distribution of the best-fit spectral parameters. The initial parameters in the MCMC chains are set to be close to the best-fit parameters obtained by the chi-squared fitting. We set a uniform prior distribution over the parameter ranges (Table 3 in Paper 1). After the initial 5000 steps are discarded to exclude the burn-in phase, further 10000 steps are explored by 1000 separate chains (“walkers”).

We succeeded in the MCMC parameter estimation for all the spectral ratios. The best-fit model ratios are shown in Appendix (Figure A.1). Blue dots in Figure 4 show the mean values obtained by the MCMC calculation. We confirmed that the best-fit parameters and their flux-dependency are similar to those by the chi-squared fitting (orange dots in Figure 4). Note that ξ is not tied among the different ratios unlike the least chi-square fitting, because the primary aim of this analysis is to ensure whether there is no correlation between v_{out} and ξ .

Figure 5 shows a corner plot of the two-dimensional correlations between the posterior distributions of the estimated parameter pairs in the spectral ratio F/A. The other corner plots are shown in Appendix, Figure A.2. We found that the velocity is not correlated with other parameters and is determined independently. In contrast, CF and ξ are correlated in most spectral ratios. Still, whereas the CF shows a clear anti-correlation with the X-ray flux, the ξ variation is tiny and will not affect the intensity variations (Figure 4).

3.3. Spectral fitting in the 0.3–10 keV band

We performed spectral fitting in 0.3–10 keV to constrain the UFO velocity with the partial absorption model based on the ratio model fitting. The spectral data are binned to have at least 20 counts per new energy bin. The XSPEC spectral model adopted is represented as

$$\text{phabs} * \text{zxcipcf} * (\text{powerlaw} + \text{diskbb}) * \text{const} * \text{kabs}, \quad (1)$$

where each spectral component is explained below.

The column density of **phabs** for the interstellar absorption was fixed at the Galactic value $N_{\text{H}} = 5 \times 10^{20} \text{ cm}^{-2}$ (Bekhti et al. 2016), where we set the cosmic abundances to the **wilms** values (Wilms et al. 2000). In addition to the model for the ratio fitting, the **kabs** model (Ueda et al. 2004, updated by Tomaru et al. 2020) is incorporated to explain the FeXXV and/or FeXXVI UFO absorption features. The **kabs** model calculates the Voigt profile absorption lines ($K\alpha$ and $K\beta$) for FeXXV and FeXXVI for the given column density of the ion N_{atom} and the turbulent velocity v_{turb} . The redshift z due to the line-of-sight velocity is also a free parameter. Although Pinto et al. (2018) reported the presence

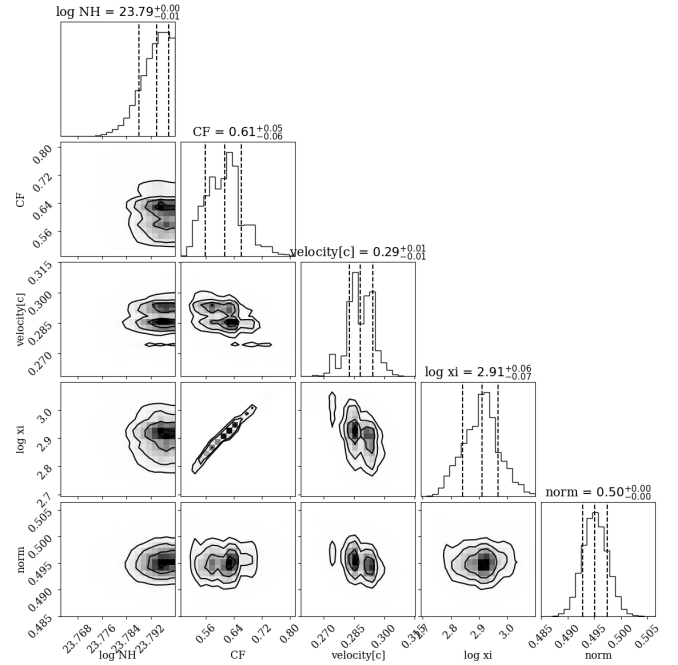


Figure 5. A corner plot showing the result of the MCMC parameter estimation for the typical spectral ratio F/A. The velocity is not correlated with other parameters, whereas a correlation is found between CF and $\log \xi$.

of O VIII UFO absorption line in the RGS spectra, we do not include the absorption line in the spectral model for simplicity. Also, disk reflection components are not required in our spectral model.

Initial parameters of the spectral fitting are set to the values constrained by the ratio model fitting. Both the continuum parameters and the partial absorption parameters were free to vary for the fitting. It is difficult to place limits on the ionization parameter and the turbulent velocity v_{turb} simultaneously from the absorption line profiles above 8 keV. Therefore, v_{turb} was fixed at 10000 km/s, and the fitting was performed assuming that the UFO absorption lines are produced either by He-like Fe or H-like Fe.

In the spectral fitting, we include $K\alpha$ and $K\beta$ lines as a pair. Three $K\alpha$ lines (accompanied by three $K\beta$ lines) at maximum are necessary to fit the UFO feature depending on the spectrum. This indicates that more than one velocity component of the UFO was observed. The fitting result of a typical intensity-sliced spectrum F is shown in Figure 6, while the others are shown in Figure A.1. Best-fit parameters are given in Table 2.

Note that our previous study based on a similar partial covering model required a strong absorption edge around 1 keV to explain the residual feature (Yamasaki et al. 2016). Now, the fit is successful without such an additional edge, which suggests that the residual feature

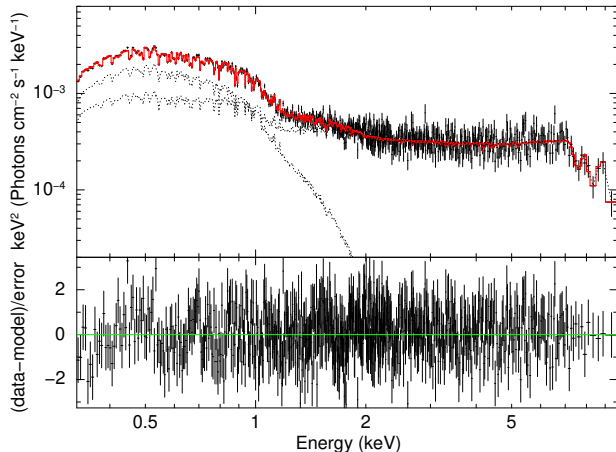


Figure 6. Spectral fitting result for the typical spectrum F in 0.3–10 keV. The dotted lines in black show `powerlaw` and `diskbb`, respectively. The red line represents the best-fit model, including three `kabs` lines at 7–10 keV. The lower panel shows the residuals of the model fitting. The other fitting results are shown in Appendix (Figure A.3).

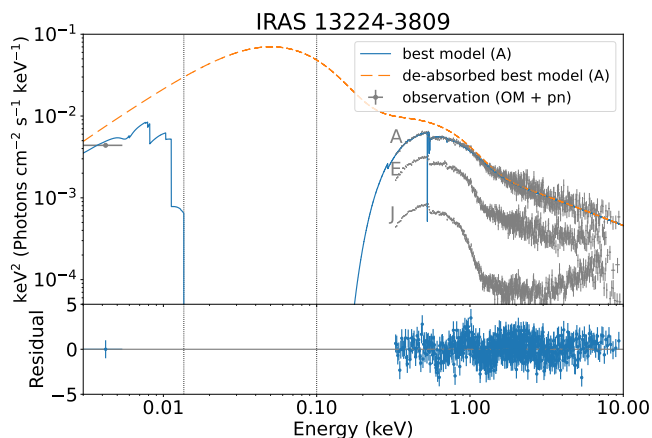


Figure 7. Broadband UV–X-ray SED fitting with pn and OM data in 3 eV–10 keV. Three intensity-sliced spectra A, E, and J are shown in gray. The blue line shows the best-fit model for spectrum A. The orange dashed line shows the deabsorbed best-fit model, from which we can estimate the intrinsic flux in UV (13.6 eV–0.1 keV) and X-rays (0.1–10.0 keV). The vertical dotted lines show the boundary of these energy bands.

was caused by the energy-shift of the *outflowing* clumpy absorbers.

3.4. SED fitting with OM+pn spectra

In this section, we model the broadband spectral energy distribution (SED) with the pn and OM data to estimate the bolometric luminosity, affecting the disk

winds and ionization degree in the ambient matter. Since we did not find significant flux variations in the OM data compared to the X-ray variation, we use the time-averaged OM spectrum.

Since IRAS 13224–3809 is a super-Eddington object and the AGN component is significant, we ignore the host galaxy contamination. In this study, we assume that spectrum A is not partially absorbed (CF=0), so we model SED of the spectrum A with the `agnslim` model (Kubota & Done 2019), multiplied by the reddening (`redden`; Cardelli et al. 1989) and the interstellar absorption (`phabs`). Here `agnslim` is a broadband spectral model for super-Eddington AGN based on the slim disk emissivity. The accretion flow is radially stratified; the inner hot Comptonization region (R_{in} to R_{hot}) with the electron temperature kT_{hot} and photon index Γ_{hot} , the intermediate warm Comptonization region to produce the soft X-ray excess (R_{warm} to R_{hot}) with the electron temperature kT_{warm} and photon index Γ_{warm} , and the outer standard disk (R_{warm} to R_{out}).

For a highly super-Eddington slim disk, the inner radius of the disk (R_{in}) is determined not only by the black hole spin but also by the gas pressure, so that R_{in} can be smaller than the inner-most stable circular orbit (Watarai et al. 2000; Kubota & Done 2019). We assume the spin parameter $a^* = 0$, and set R_{in} to the radius calculated by Kubota & Done (2019) (see Equation 1 in their paper). We also fixed the column density of the interstellar absorption N_{H} to $5 \times 10^{20} \text{ cm}^{-2}$ and $E(B - V) = 1.7 \times N_{\text{H}}/10^{22} \text{ cm}^{-2}$ (Bohlin et al. 1978).

The averaged OM spectrum and pn spectrum A are successfully fitted with the assumed model. Figure 7 shows the νf_{ν} plot of the broadband SED in 3 eV–10 keV. The gray lines indicate the three representative intensity-sliced spectra A, E, and J, and the blue line represents the best-fit SED model for spectrum A. Best-fit parameters are given in Table 3.

4. DISCUSSION

4.1. Comparison between the UFO and clumpy absorbers

In Section 3, we constrained the outflow velocity, v_{out} , of the partial clumpy absorbers using the unique spectral ratio fitting method. We also performed the conventional spectral fitting to determine the v_{out} of the UFO. Comparison of the outflow velocities of the UFOs and partial absorbers are shown in Figure 8, where these velocities are plotted against the 3.0–10.0 keV X-ray flux of the intensity-sliced spectra. When a UFO is composed of multiple absorption lines with different velocity components, the average velocity weighted by the column density of each absorption line (N_{atom}) is plotted.

Table 2. Best-fit parameters determined by the spectral fitting in 0.3–10.0 keV. The CF of `zxicpf` and `const` are fixed to the values determined by the chi-squared ratio fitting (upper panel of Table 1). Fitting was made assuming that the UFO absorption lines are produced either by He-like Fe or H-like Fe. The parameters except `kabs` are determined assuming the He-like Fe. Fitting results are shown in Figure A.3. Hereafter the error ranges correspond to the 90% confidence level.

Components	Parameters	A	B	C	D	E
<code>zxicpf</code>	N_{H} (10^{22}cm^{-2})	—	36_{-7}^{+13}	46_{-6}^{+9}	51_{-5}^{+4}	56_{-5}^{+5}
	$\log \xi$	—	$2.72_{-0.04}^{+0.04}$	$2.73_{-0.05}^{+0.03}$	$2.73_{-0.11}^{+0.05}$	$2.72_{-0.03}^{+0.03}$
	z	—	$-0.33_{-0.02}^{+0.01}$	$-0.33_{-0.01}^{+0.01}$	$-0.32_{-0.01}^{+0.01}$	$-0.32_{-0.01}^{+0.01}$
<code>powerlaw</code>	Γ	$2.67_{-0.03}^{+0.03}$	$2.71_{-0.03}^{+0.03}$	$2.60_{-0.03}^{+0.03}$	$2.60_{-0.04}^{+0.03}$	$2.54_{-0.03}^{+0.03}$
	norm (10^{-3})	$2.2_{-0.1}^{+0.1}$	$2.3_{-0.1}^{+0.1}$	$2.2_{-0.1}^{+0.1}$	$2.3_{-0.2}^{+0.1}$	$2.4_{-0.1}^{+0.1}$
<code>diskbb</code>	kT_{in} (eV)	182_{-1}^{+1}	178_{-2}^{+2}	177_{-2}^{+2}	179_{-3}^{+2}	177_{-2}^{+2}
	norm	731_{-33}^{+34}	757_{-62}^{+45}	845_{-55}^{+46}	781_{-57}^{+89}	831_{-59}^{+72}
<i>Assuming Fe XXV</i>						
<code>kabs</code>	$N_{\text{Fe XXV}}$ (10^{18}cm^{-2})	—	2_{-1}^{+2}	4_{-1}^{+2}	4_{-1}^{+2}	5_{-2}^{+2}
	z	—	$-0.26_{-0.10}^{+0.04}$	$-0.29_{-0.02}^{+0.03}$	$-0.24_{-0.02}^{+0.01}$	$-0.25_{-0.02}^{+0.02}$
<code>kabs</code>	$N_{\text{Fe XXV}}$ (10^{18}cm^{-2})	—	—	—	8_{-3}^{+6}	6_{-2}^{+5}
	z	—	—	—	$-0.33_{-0.01}^{+0.01}$	$-0.32_{-0.02}^{+0.02}$
<code>kabs</code>	$N_{\text{Fe XXV}}$ (10^{18}cm^{-2})	—	—	—	—	—
	z	—	—	—	—	—
<i>Assuming Fe XXVI</i>						
<code>kabs</code>	$N_{\text{Fe XXVI}}$ (10^{18}cm^{-2})	—	4_{-3}^{+4}	7_{-3}^{+5}	8_{-3}^{+4}	10_{-4}^{+5}
	z	—	$-0.23_{-0.11}^{+0.04}$	$-0.26_{-0.02}^{+0.03}$	$-0.21_{-0.02}^{+0.01}$	$-0.22_{-0.02}^{+0.02}$
<code>kabs</code>	$N_{\text{Fe XXVI}}$ (10^{18}cm^{-2})	—	—	—	17_{-7}^{+12}	12_{-5}^{+9}
	z	—	—	—	$-0.30_{-0.01}^{+0.01}$	$-0.29_{-0.01}^{+0.02}$
<code>kabs</code>	$N_{\text{Fe XXVI}}$ (10^{18}cm^{-2})	—	—	—	—	—
	z	—	—	—	—	—
χ^2/dof		760.5/677	731.3/628	715.4/639	616.7/608	747.9/619
Components	Parameters	F	G	H	I	J
<code>zxicpf</code>	N_{H} (10^{22}cm^{-2})	52_{-5}^{+6}	56_{-5}^{+5}	54_{-4}^{+4}	57_{-4}^{+4}	60_{-3}^{+3}
	$\log \xi$	$2.76_{-0.16}^{+0.04}$	$2.78_{-0.03}^{+0.03}$	$2.81_{-0.03}^{+0.03}$	$2.85_{-0.02}^{+0.02}$	$2.91_{-0.02}^{+0.02}$
	z	$-0.31_{-0.01}^{+0.01}$	$-0.31_{-0.01}^{+0.01}$	$-0.30_{-0.01}^{+0.01}$	$-0.29_{-0.01}^{+0.01}$	$-0.28_{-0.01}^{+0.00}$
<code>powerlaw</code>	Γ	$2.47_{-0.04}^{+0.04}$	$2.40_{-0.04}^{+0.04}$	$2.34_{-0.04}^{+0.04}$	$2.24_{-0.05}^{+0.05}$	$1.95_{-0.05}^{+0.05}$
	norm (10^{-3})	$2.2_{-0.2}^{+0.3}$	$2.2_{-0.2}^{+0.2}$	$2.0_{-0.2}^{+0.2}$	$1.8_{-0.2}^{+0.2}$	$1.2_{-0.1}^{+0.1}$
<code>diskbb</code>	kT_{in} (eV)	173_{-2}^{+2}	170_{-2}^{+2}	168_{-1}^{+2}	165_{-1}^{+1}	165_{-1}^{+1}
	norm	986_{-99}^{+85}	1085_{-89}^{+85}	1238_{-83}^{+83}	1406_{-78}^{+77}	1589_{-62}^{+63}
<i>Assuming Fe XXV</i>						
<code>kabs</code>	$N_{\text{Fe XXV}}$ (10^{18}cm^{-2})	3_{-1}^{+1}	2_{-1}^{+1}	8_{-2}^{+3}	3_{-1}^{+1}	7_{-1}^{+2}
	z	$-0.18_{-0.02}^{+0.01}$	$-0.14_{-0.02}^{+0.02}$	$-0.24_{-0.01}^{+0.01}$	$-0.20_{-0.01}^{+0.01}$	$-0.22_{-0.01}^{+0.01}$
<code>kabs</code>	$N_{\text{Fe XXV}}$ (10^{18}cm^{-2})	5_{-1}^{+2}	10_{-2}^{+3}	6_{-2}^{+4}	7_{-2}^{+3}	7_{-2}^{+4}
	z	$-0.25_{-0.01}^{+0.01}$	$-0.23_{-0.01}^{+0.01}$	$-0.32_{-0.02}^{+0.01}$	$-0.26_{-0.01}^{+0.01}$	$-0.31_{-0.01}^{+0.01}$
<code>kabs</code>	$N_{\text{Fe XXV}}$ (10^{18}cm^{-2})	9_{-3}^{+26}	5_{-2}^{+3}	—	3_{-1}^{+2}	—
	z	$-0.34_{-0.04}^{+0.01}$	$-0.31_{-0.02}^{+0.02}$	—	$-0.33_{-0.02}^{+0.02}$	—
<i>Assuming Fe XXVI</i>						
<code>kabs</code>	$N_{\text{Fe XXVI}}$ (10^{18}cm^{-2})	6_{-2}^{+3}	5_{-2}^{+2}	16_{-4}^{+7}	7_{-3}^{+3}	16_{-3}^{+5}
	z	$-0.14_{-0.02}^{+0.02}$	$-0.10_{-0.02}^{+0.02}$	$-0.21_{-0.01}^{+0.01}$	$-0.16_{-0.01}^{+0.01}$	$-0.19_{-0.01}^{+0.01}$
<code>kabs</code>	$N_{\text{Fe XXVI}}$ (10^{18}cm^{-2})	11_{-3}^{+5}	20_{-4}^{+7}	13_{-5}^{+9}	15_{-5}^{+7}	16_{-4}^{+8}
	z	$-0.22_{-0.01}^{+0.01}$	$-0.20_{-0.01}^{+0.01}$	$-0.29_{-0.02}^{+0.01}$	$-0.22_{-0.01}^{+0.01}$	$-0.29_{-0.01}^{+0.01}$
<code>kabs</code>	$N_{\text{Fe XXVI}}$ (10^{18}cm^{-2})	18_{-6}^{+45}	10_{-4}^{+7}	—	6_{-3}^{+4}	—
	z	$-0.31_{-0.03}^{+0.01}$	$-0.28_{-0.02}^{+0.02}$	—	$-0.30_{-0.02}^{+0.02}$	—
χ^2/dof		676.4/625	712.9/624	766.9/629	665.8/612	779.4/642

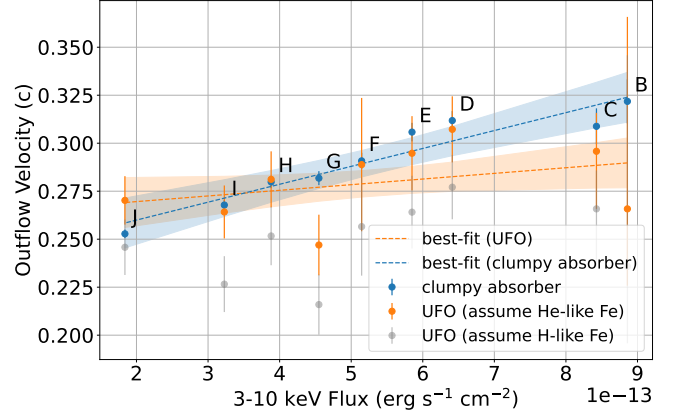
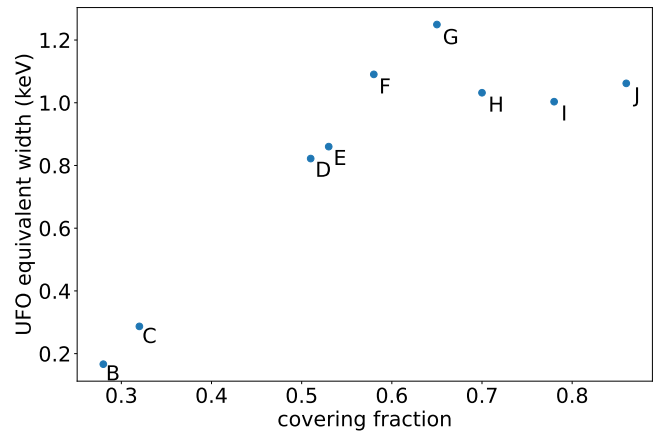
Table 3. Best-fit parameters determined by the SED fitting obtained by OM and pn.

Components	Parameters	Best-fit values
phabs	N_{H} (10^{20} cm^{-2})	5 (fixed)
redden	$E(B - V)$	0.086 (fixed)
agnslim	mass (M_{\odot})	5.4×10^6 (fixed)
	\dot{M} (\dot{M}_{Edd})	6.30 ± 0.01
	a^*	0 (fixed)
	$\cos i$	0.5 (fixed)
	kT_{hot} (keV)	100 (fixed)
	kT_{warm} (keV)	0.166 ± 0.005
	Γ_{hot}	2.67 ± 0.04
	Γ_{warm}	$1.66^{+0.09}_{-0.10}$
	R_{hot} (R_{g})	8.3 ± 0.2
	R_{warm} (R_{g})	10.6 ± 0.1

We fitted the velocities of the UFOs and clumpy absorbers as a function of the X-ray flux with linear functions. The orange and blue dotted lines in Figure 8 show the best-fit models with 1σ uncertainties. Although the slopes of the two best-fit functions are slightly different, we see similar increasing trends with the X-ray flux of the clump velocities and the UFO velocities either assuming the He-like or H-like absorption lines. In particular, the orange dots in Figure 8 assuming the He-like Fe absorption show similar velocity values with those of the clumpy absorbers. This finding is consistent with the “hot inner and clumpy outer wind” scenario by Mizumoto et al. (2019), where the outer clumpy absorbers are the consequence of the inner hot UFO winds.

If the proposed scenario is valid, there should be a correlation between the clumps and UFOs along the line of sight. To investigate this possibility, we plotted the clump covering fraction (see Table 1) and the equivalent width of the UFO absorption lines (Figure 9). The equivalent width was calculated as the sum of the individual equivalent widths of multiple absorption lines. Figure 9 indicates a clear correlation between the two variables, in particular a surprising linearity in the B–G range. This finding suggests a simple fact that more material in the line-of-sight will result in more prominent UFOs and partial covering, providing further evidence of the “hot inner and clumpy outer wind” scenario.

These results have also been suggested in PDS 456, which is another super-Eddington source. Matzeu et al. (2016) searched for the outflow velocity of the clumpy absorber to give the best spectral fit, and reported the global minimum solution at a velocity of $0.25 c$. Matzeu et al. (2017) also found in the same target that the centroid energy of Fe K UFO absorption increases with the


Figure 8. Outflow velocities of the clumpy absorbers (in blue) obtained from the spectral ratio fitting, and those of the UFOs estimated from the spectral fitting (in orange and gray assuming He-like and H-like iron, respectively). The outflowing velocities are plotted against the 3-10 keV flux of the intensity-sliced spectra. The blue and orange dotted lines show the best-fit linear functions of the UFOs and clumps with 1σ uncertainties.

Figure 9. The horizontal axis shows the clump covering fraction, and the vertical axis shows the equivalent width of the UFO absorption lines, which is calculated as the sum of individual equivalent widths of multiple absorption lines.

ionizing flux. Reeves et al. (2021) similarly explained the spectrum of PDS 456 in terms of the partial absorption; Figure 16 in their paper clearly shows that the UFO absorption lines are more prominent when the soft X-rays are more significantly absorbed by the partial clumps.

4.2. Relation of variations between intrinsic UV/X-ray luminosity and UFO velocity

As shown in Figure 1, the observed $0.3 - 10$ keV flux variation ranges over more than one order of magnitude. On the other hand, the ratio fitting results show that the intrinsic X-ray flux is varied by only a factor of ~ 4 , indicating that a considerable amount of the apparent

flux variation is caused by changes in the partial covering fraction.

The orange dashed line in Figure 7 shows the deabsorbed UV-X-ray spectrum for spectrum A in which the covering fraction is assumed to be null. From this deabsorbed model, the intrinsic UV flux in 13.6 eV – 0.1 keV and the intrinsic X-ray flux in 0.1–10.0 keV are estimated respectively to be 1.8×10^{-10} erg cm⁻² s⁻¹ and 6.1×10^{-11} erg cm⁻² s⁻¹, using `flux` command in XSPEC. The proportion of the intrinsic UV flux to X-ray flux is approximately 3 : 1. Since the intrinsic X-ray flux varies by a factor of ~ 4 while the UV flux is invariable, the total flux variation of UV and X-rays can be estimated to be about a factor of $\sim 16/13$, assuming that the obtained ratio (UV flux: X-ray flux = 3:1) is valid throughout the observation period.

In case the disk wind is driven by continuum radiation, the total flux variation is expected to contribute directly to the increase in the kinetic energy of the disk wind. Since the outflow velocity is proportional to the square root of the wind kinetic energy, the velocity change is estimated to be about a factor of $\sqrt{16/13} \sim 1.1$.

By extrapolating the best-fit model in Figure 8, the velocities of the UFO and clumpy absorbers in spectrum A (1.4×10^{-12} erg cm⁻² s⁻¹ in 3–10 keV) are estimated to be 0.31 c and 0.37 c . As a result, the variations of the UFO and clump velocities from the dimmest spectrum (J) to the brightest one (A) are about a factor of 1.1 and 1.4, respectively. These values are consistent with the simple estimation above, thus both the clumpy absorbers and the UFOs are considered to be driven by the same UV-dominant continuum radiation.

4.3. Constant ionization parameter of the clumps

Ionization parameter ($\xi = L/nr^2$) values of the clumpy absorbers determined from the model fitting are hardly variable regardless of the X-ray flux (Table 1 and 2). This fact suggests that the gas density of the clump, n , increases or that the location where the clump is formed, r , gets more distant as the X-ray luminosity increases.

Takeuchi et al. (2014) suggests that the clump is formed by a sort of radiation hydrodynamic instability in addition to the Rayleigh-Taylor instability. The radiation instability should work only at a certain opacity, i.e., a certain ξ . If the instability is activated and the clumps are produced at this specific distance which increases with the luminosity, the result that ξ being constant is reasonable. This may be a common feature of the super-Eddington objects with continuum-driven outflows. It will be intriguing to investigate the flux

dependence of ξ in other super-Eddington sources in future.

4.4. Explanation of other observed properties

IRAS 13224–3809 has been observed many times and extensively investigated to date. This section will discuss how our model can explain these observed properties of IRAS 13224–3809.

In our model, spectral variability is explained by the variation of the PL continuum component and the partial absorption component. On the other hand, Parker et al. (2017) used the principle component analysis (PCA) to decompose the spectral variability, and argued that the PL emission dominates the spectral variability, with a minor contribution from the reflection and UFO component. The PCA is a powerful data science tool to reduce the dimensionality of the input data, but one must be careful with its applicability in X-ray spectral analysis. Pike et al. (2017) performed a spectral component decomposition of the simulated X-ray spectral variations of NLS1 galaxies using the PCA and the non-negative matrix factorization (NMF). Despite the PCA’s good performance in determining the number of the independent spectral components, the decomposed components derived by the PCA include the *negative* values as residuals from the average spectrum, being very different from the original components. The other method, NMF, has the advantage of being composed of non-negative values, making it easier to interpret the spectral components, in particular when the variable components are *additive*. Still, NMF is not very useful when variable spectral components are *multiplicative*, just like our model. We expect that forthcoming analyses using new techniques will reveal the main cause of the spectral variation without prior assumptions.

X-ray observations provide not only spectroscopic information but also timing information. Characteristic power spectral density (PSD) and soft/hard lags have been reported in IRAS 13224–3809. The PSD peaks at timescales of about 30 ks (e.g., Alston et al. 2019). The radiation-magnetohydrodynamic simulations suggest the clumpy absorbers to exist at a few hundred R_s from the center (Takeuchi et al. 2013). Assuming the clump exists at 500 R_s , the Keplerian rotation period is calculated to be about 200 ks. Since the typical clump size is around 10 R_s (Takeuchi et al. 2013), a variation of 30 ks is reasonable with our model in terms of changes in the partial covering fraction.

The “lag-frequency plot” can be derived from the light curves of the primary X-ray emission (typically 1.0–4.0 keV) and the soft excess (below ~ 1.0 keV). In this plot, a hard lag is observed in the low-frequency band

below 10^{-4} Hz, while a soft lag is observed in the high-frequency band above 10^{-3} Hz (e.g., De Marco et al. 2013 and Alston et al. 2020). The low-frequency hard lag has a PL-like shape and decreases with frequency. This is considered to be due to inward propagation of the fluctuations through the accretion flow and corona (e.g., Arévalo & Uttley 2006).

Since the mechanism of the soft X-ray excess has not yet been clearly understood, two major hypotheses exist as to the cause of the high-frequency soft lag. One is reverberation due to reflection by the inner region of the accretion disk around $\sim 10 R_s$ (e.g., Fabian et al. 2009 and Zoghbi et al. 2012), where the reprocessed emission is delayed by the light travel time from the source. The other hypothesis says that the lag is a solely mathematical artifact due to phase wrapping (Miller et al. 2010a; Legg et al. 2012; Mizumoto et al. 2019), which is also favored by our model.

When examining the energy dependence of the lag in the high-frequency range where the soft lag is observed, a significant peak structure is often found in the Fe K band. This is thought to be caused by the primary X-rays scattering off the surrounding material, generating the Fe emission lines with a reverberation lag (e.g., Zoghbi et al. 2012 and Kara et al. 2013). If this lag is literally taken as the light propagation time due to the reflection in the inner accretion disk, the size is about $10 R_s$. On the other hand, if we take into account the dilution effect due to the weaker iron emission line compared to the continuum, the lag can be attributed to the reflections from the materials located as far away as $\sim 100 R_s$ (e.g., Miller et al. 2010b). We speculate that the scattering by the disk wind in our model at $\sim 100 R_s$ can explain the observed reverberation lag (Mizumoto et al. 2018, 2019).

X-ray light curves of almost any kinds of accreting objects, including AGNs, exhibit a linear relationship between the root mean square (RMS) amplitude and the flux variations (e.g., Uttley & McHardy 2001 and Alston et al. 2019). The fact that this relationship has been observed for any objects with accretion disks suggests that it is due to intrinsic X-ray variability, not due to apparent absorption effects. We suppose that the intrinsic PL variability in our model is responsible for this relation, while quantitative estimation is a future subject.

5. CONCLUSION

We have applied the unique “spectral-ratio model fitting” technique for the first time to disentangle spectral model/parameter degeneracy of the NLS1 IRAS 13224–3809. Taking the spectral ratios of the intensity-sliced spectra allows us to focus on variable absorption features by canceling the time-invariable continuum and other absorption components. Consequently, we found that the soft X-ray spectral variation is mostly explained by the change in the covering fraction of the mildly-ionized clumpy absorbers, and that the clumps are outflowing at noticeably high velocities comparable to those of UFOs (~ 0.2 – $0.3 c$).

We found that both velocities of the partially absorbing clumps and the UFOs increase with the intrinsic UV-X-ray luminosity, and the luminosity dependence suggests that the outflowing velocity being consistent with the kinetic velocity of the radiatively driven winds. This is the first observational evidence that the clumps responsible for the partial absorption have the same origin as the radiation-driven UFOs. Present results support the “hot inner and clumpy outer wind” scenario (Mizumoto et al. 2019), where the clumpy absorbers are originated from the inner hot UFO winds driven by the UV-dominant continuum radiation.

This research has used data and software provided by the High Energy Astrophysics Science Archive Research Center (HEASARC), a service of the Astrophysics Science Division at NASA/GSFC and the High Energy Astrophysics Division of the Smithsonian Astrophysical Observatory. This study was based on observations obtained with *XMM-Newton*, ESA science missions with instruments and contributions directly funded by ESA Member States and NASA. This research was supported by JSPS Grant-in-Aid for JSPS Research Fellow Grant Number JP20J20809 (T.M.), JSPS KAKENHI Grant Number JP21K13958 (M.M). M.M. acknowledges support from the Hakubi project at Kyoto University.

Facilities: XMM-Newton(pn, OM)

Software: XSTAR (Kallman & Bautista 2001; Kallman et al. 2004), XSPEC (Arnaud 1996), SAS (Gabriel et al. 2004)

REFERENCES

- Alston, W. N., Fabian, A. C., Buisson, D. J. K., et al. 2019, Monthly Notices of the Royal Astronomical Society, 482, 2088, doi: [10.1093/mnras/sty2527](https://doi.org/10.1093/mnras/sty2527)
- Alston, W. N., Fabian, A. C., Kara, E., et al. 2020, Nature Astronomy, 4, 597, doi: [10.1038/s41550-019-1002-x](https://doi.org/10.1038/s41550-019-1002-x)

- Arévalo, P., & Uttley, P. 2006, *Monthly Notices of the Royal Astronomical Society*, 367, 801, doi: [10.1111/j.1365-2966.2006.09989.x](https://doi.org/10.1111/j.1365-2966.2006.09989.x)
- Arnaud, K. A. 1996, *Astronomical Data Analysis Software and Systems*, 101, 17
- Bekhti, N. B., Flöer, L., Keller, R., et al. 2016, *Astronomy & Astrophysics*, 594, A116, doi: [10.1051/0004-6361/201629178](https://doi.org/10.1051/0004-6361/201629178)
- Bohlin, R. C., Savage, B. D., & Drake, J. F. 1978, *The Astrophysical Journal*, 224, 132, doi: [10.1086/156357](https://doi.org/10.1086/156357)
- Cardelli, J. A., Clayton, G. C., & Mathis, J. S. 1989, *The Astrophysical Journal*, 345, 245, doi: [10.1086/167900](https://doi.org/10.1086/167900)
- Chartas, G., & Canas, M. H. 2018, *The Astrophysical Journal*, 867, 103, doi: [10.3847/1538-4357/aae438](https://doi.org/10.3847/1538-4357/aae438)
- Chiang, C.-Y., Walton, D. J., Fabian, A. C., Wilkins, D. R., & Gallo, L. C. 2015, *Monthly Notices of the Royal Astronomical Society*, 446, 759, doi: [10.1093/mnras/stu2087](https://doi.org/10.1093/mnras/stu2087)
- Dannen, R. C., Proga, D., Waters, T., & Dyda, S. 2020, *The Astrophysical Journal*, 893, L34, doi: [10.3847/2041-8213/ab87a5](https://doi.org/10.3847/2041-8213/ab87a5)
- De Marco, B., Ponti, G., Cappi, M., et al. 2013, *Monthly Notices of the Royal Astronomical Society*, 431, 2441, doi: [10.1093/mnras/stt339](https://doi.org/10.1093/mnras/stt339)
- Di Gesu, L., Costantini, E., Ebrero, J., et al. 2015, *Astronomy and Astrophysics*, 579, A42, doi: [10.1051/0004-6361/201525934](https://doi.org/10.1051/0004-6361/201525934)
- Emmanoulopoulos, D., Papadakis, I. E., Dovčiak, M., & McHardy, I. M. 2014, *Monthly Notices of the Royal Astronomical Society*, 439, 3931, doi: [10.1093/mnras/stu249](https://doi.org/10.1093/mnras/stu249)
- Fabian, A. C., Rees, M. J., Stella, L., & White, N. E. 1989, *Monthly Notices of the Royal Astronomical Society*, 238, 729, doi: [10.1093/mnras/238.3.729](https://doi.org/10.1093/mnras/238.3.729)
- Fabian, A. C., Zoghbi, A., Ross, R. R., et al. 2009, *Nature*, 459, 540, doi: [10.1038/nature08007](https://doi.org/10.1038/nature08007)
- Fabian, A. C., Kara, E., Walton, D. J., et al. 2013, *Monthly Notices of the Royal Astronomical Society*, 429, 2917, doi: [10.1093/mnras/sts504](https://doi.org/10.1093/mnras/sts504)
- Foreman-Mackey, D., Hogg, D. W., Lang, D., & Goodman, J. 2013, *Publications of the Astronomical Society of the Pacific*, 125, 306, doi: [10.1086/670067](https://doi.org/10.1086/670067)
- Gabriel, C., Denby, M., Fyfe, D. J., et al. 2004, 314, 759
- Gofford, J., Reeves, J. N., Tombesi, F., et al. 2013, *Monthly Notices of the Royal Astronomical Society*, 430, 60, doi: [10.1093/mnras/sts481](https://doi.org/10.1093/mnras/sts481)
- Hagino, K., Odaka, H., Done, C., et al. 2015, *Monthly Notices of the Royal Astronomical Society*, 446, 663, doi: [10.1093/mnras/stu2095](https://doi.org/10.1093/mnras/stu2095)
- Igo, Z., Parker, M. L., Matzeu, G. A., et al. 2020, *Monthly Notices of the Royal Astronomical Society*, 493, 1088, doi: [10.1093/mnras/staa265](https://doi.org/10.1093/mnras/staa265)
- Jansen, F., Lumb, D., Altieri, B., et al. 2001, *Astronomy & Astrophysics*, 365, L1, doi: [10.1051/0004-6361:20000036](https://doi.org/10.1051/0004-6361:20000036)
- Jiang, J., Dauser, T., Fabian, A. C., et al. 2022, arXiv:2204.09908 [astro-ph]. <http://ascl.net/2204.09908>
- Kaastra, J. S., Kriss, G. A., Cappi, M., et al. 2014, *Science*, 345, 64, doi: [10.1126/science.1253787](https://doi.org/10.1126/science.1253787)
- Kallman, T., & Bautista, M. 2001, *The Astrophysical Journal Supplement Series*, 133, 221, doi: [10.1086/319184](https://doi.org/10.1086/319184)
- Kallman, T. R., Palmeri, P., Bautista, M. A., Mendoza, C., & Krolik, J. H. 2004, *The Astrophysical Journal Supplement Series*, 155, 675, doi: [10.1086/424039](https://doi.org/10.1086/424039)
- Kara, E., Fabian, A. C., Cackett, E. M., et al. 2013, *Monthly Notices of the Royal Astronomical Society*, 428, 2795, doi: [10.1093/mnras/sts155](https://doi.org/10.1093/mnras/sts155)
- King, A. 2010, *Monthly Notices of the Royal Astronomical Society*, 402, 1516, doi: [10.1111/j.1365-2966.2009.16013.x](https://doi.org/10.1111/j.1365-2966.2009.16013.x)
- King, A., & Pounds, K. 2015, *Annual Review of Astronomy and Astrophysics*, 53, 115, doi: [10.1146/annurev-astro-082214-122316](https://doi.org/10.1146/annurev-astro-082214-122316)
- Kobayashi, H., Ohsuga, K., Takahashi, H. R., et al. 2018, *Publications of the Astronomical Society of Japan*, 70, 22, doi: [10.1093/pasj/psx157](https://doi.org/10.1093/pasj/psx157)
- Kubota, A., & Done, C. 2019, *Monthly Notices of the Royal Astronomical Society*, 489, 524, doi: [10.1093/mnras/stz2140](https://doi.org/10.1093/mnras/stz2140)
- Laha, S., Guainazzi, M., Dewangan, G. C., Chakravorty, S., & Kembhavi, A. K. 2014, *Monthly Notices of the Royal Astronomical Society*, 441, 2613, doi: [10.1093/mnras/stu669](https://doi.org/10.1093/mnras/stu669)
- Laha, S., Reynolds, C. S., Reeves, J., et al. 2021, *Nature Astronomy*, 5, 13, doi: [10.1038/s41550-020-01255-2](https://doi.org/10.1038/s41550-020-01255-2)
- Legg, E., Miller, L., Turner, T. J., et al. 2012, *The Astrophysical Journal*, 760, 73, doi: [10.1088/0004-637X/760/1/73](https://doi.org/10.1088/0004-637X/760/1/73)
- Mason, K. O., Breeveld, A., Much, R., et al. 2001, *Astronomy & Astrophysics*, 365, L36, doi: [10.1051/0004-6361:20000044](https://doi.org/10.1051/0004-6361:20000044)
- Matzeu, G. A., Reeves, J. N., Braitto, V., et al. 2017, *Monthly Notices of the Royal Astronomical Society: Letters*, 472, L15, doi: [10.1093/mnrasl/slx129](https://doi.org/10.1093/mnrasl/slx129)
- Matzeu, G. A., Reeves, J. N., Nardini, E., et al. 2016, *Monthly Notices of the Royal Astronomical Society*, 458, 1311, doi: [10.1093/mnras/stw354](https://doi.org/10.1093/mnras/stw354)
- Matzeu, G. A., Brusa, M., Lanzuisi, G., et al. 2023, *Astronomy & Astrophysics*, 670, A182, doi: [10.1051/0004-6361/202245036](https://doi.org/10.1051/0004-6361/202245036)

- McKernan, B., Yaqoob, T., & Reynolds, C. S. 2007, *Monthly Notices of the Royal Astronomical Society*, 379, 1359, doi: [10.1111/j.1365-2966.2007.11993.x](https://doi.org/10.1111/j.1365-2966.2007.11993.x)
- Midooka, T., Ebisawa, K., Mizumoto, M., & Sugawara, Y. 2022a, *Monthly Notices of the Royal Astronomical Society*, stac1206, doi: [10.1093/mnras/stac1206](https://doi.org/10.1093/mnras/stac1206)
- Midooka, T., Mizumoto, M., & Ebisawa, K. 2022b
- Miller, L., Turner, T. J., Reeves, J. N., & Braitto, V. 2010a, *Monthly Notices of the Royal Astronomical Society*, 408, 1928, doi: [10.1111/j.1365-2966.2010.17261.x](https://doi.org/10.1111/j.1365-2966.2010.17261.x)
- Miller, L., Turner, T. J., Reeves, J. N., et al. 2010b, *Monthly Notices of the Royal Astronomical Society*, 403, 196, doi: [10.1111/j.1365-2966.2009.16149.x](https://doi.org/10.1111/j.1365-2966.2009.16149.x)
- Mizumoto, M., Done, C., Hagino, K., et al. 2018, *Monthly Notices of the Royal Astronomical Society*, 478, 971, doi: [10.1093/mnras/sty1114](https://doi.org/10.1093/mnras/sty1114)
- Mizumoto, M., Ebisawa, K., Tsujimoto, M., et al. 2019, *Monthly Notices of the Royal Astronomical Society*, 482, 5316, doi: [10.1093/mnras/sty3056](https://doi.org/10.1093/mnras/sty3056)
- Nardini, E., Reeves, J. N., Gofford, J., et al. 2015, *Science*, 347, 860, doi: [10.1126/science.1259202](https://doi.org/10.1126/science.1259202)
- Parker, M. L., Matzeu, G. A., Matthews, J. H., et al. 2022, *Monthly Notices of the Royal Astronomical Society*, 513, 551, doi: [10.1093/mnras/stac877](https://doi.org/10.1093/mnras/stac877)
- Parker, M. L., Pinto, C., Fabian, A. C., et al. 2017, *Nature*, 543, 83, doi: [10.1038/nature21385](https://doi.org/10.1038/nature21385)
- Pike, S., Ebisawa, K., Ikeda, S., et al. 2017, *Journal of Space Science Informatics Japan*, 6, 73, doi: <https://doi.org/10.20637/JAXA-RR-16-007/0007>
- Pinto, C., Alston, W., Parker, M. L., et al. 2018, *Monthly Notices of the Royal Astronomical Society*, 476, 1021, doi: [10.1093/mnras/sty231](https://doi.org/10.1093/mnras/sty231)
- Reeves, J., Done, C., Pounds, K., et al. 2008, *Monthly Notices of the Royal Astronomical Society*, 385, L108, doi: [10.1111/j.1745-3933.2008.00443.x](https://doi.org/10.1111/j.1745-3933.2008.00443.x)
- Reeves, J. N., Braitto, V., Porquet, D., et al. 2021, *Monthly Notices of the Royal Astronomical Society*, 500, 1974, doi: [10.1093/mnras/staa3377](https://doi.org/10.1093/mnras/staa3377)
- Strüder, L., Briel, U., Dennerl, K., et al. 2001, *Astronomy & Astrophysics*, 365, L18, doi: [10.1051/0004-6361:20000066](https://doi.org/10.1051/0004-6361:20000066)
- Takeuchi, S., Ohsuga, K., & Mineshige, S. 2013, *Publications of the Astronomical Society of Japan*, 65, 88, doi: [10.1093/pasj/65.4.88](https://doi.org/10.1093/pasj/65.4.88)
- . 2014, *Publications of the Astronomical Society of Japan*, 66, 48, doi: [10.1093/pasj/psu011](https://doi.org/10.1093/pasj/psu011)
- Tomaru, R., Done, C., Ohsuga, K., Odaka, H., & Takahashi, T. 2020, *Monthly Notices of the Royal Astronomical Society*, 494, 3413, doi: [10.1093/mnras/staa961](https://doi.org/10.1093/mnras/staa961)
- Tombesi, F., Cappi, M., Reeves, J. N., et al. 2010, *Astronomy and Astrophysics*, 521, A57, doi: [10.1051/0004-6361/200913440](https://doi.org/10.1051/0004-6361/200913440)
- Ueda, Y., Murakami, H., Yamaoka, K., Dotani, T., & Ebisawa, K. 2004, *The Astrophysical Journal*, 609, 325, doi: [10.1086/420973](https://doi.org/10.1086/420973)
- Uttley, P., & McHardy, I. M. 2001, *Monthly Notices of the Royal Astronomical Society*, 323, L26, doi: [10.1046/j.1365-8711.2001.04496.x](https://doi.org/10.1046/j.1365-8711.2001.04496.x)
- Watarai, K.-y., Fukue, J., Takeuchi, M., & Mineshige, S. 2000, *Publications of the Astronomical Society of Japan*, 52, 133, doi: [10.1093/pasj/52.1.133](https://doi.org/10.1093/pasj/52.1.133)
- Wilms, J., Allen, A., & McCray, R. 2000, *The Astrophysical Journal*, 542, 914, doi: [10.1086/317016](https://doi.org/10.1086/317016)
- Yamasaki, H., Mizumoto, M., Ebisawa, K., & Sameshima, H. 2016, *Publications of the Astronomical Society of Japan*, 68, 80, doi: [10.1093/pasj/psw070](https://doi.org/10.1093/pasj/psw070)
- Zhang, J.-X., Wang, J.-X., & Zhu, F.-F. 2018, *The Astrophysical Journal*, 863, 71, doi: [10.3847/1538-4357/aac92](https://doi.org/10.3847/1538-4357/aac92)
- Zoghbi, A., Fabian, A. C., Reynolds, C. S., & Cackett, E. M. 2012, *Monthly Notices of the Royal Astronomical Society*, 422, 129, doi: [10.1111/j.1365-2966.2012.20587.x](https://doi.org/10.1111/j.1365-2966.2012.20587.x)

APPENDIX

A. ADDITIONAL PLOTS

Three additional plots are given in Appendix. First, the MCMC fitting results for all the nine spectra ratios (Figure A.1). Second, all the MCMC contour plots are shown in Figure A.2, where none of the parameters correlate with the velocity, which indicates that the velocity is independently determined. Finally, Figure A.3 shows all the spectral fitting results, which are successful including the complex UFO features.

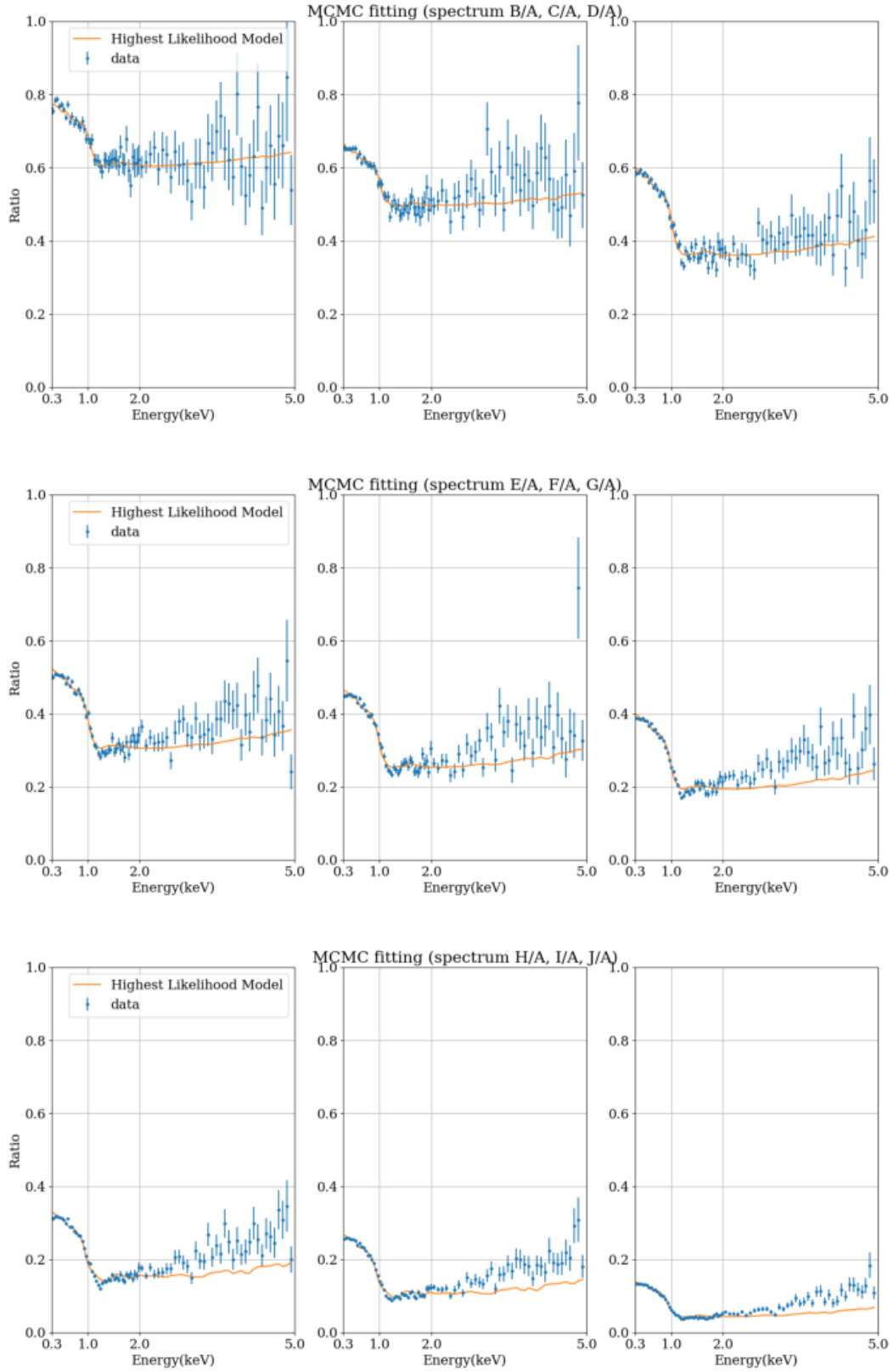


Figure A.1. MCMC fitting results of all the spectral ratios.

IRAS 13224-3809

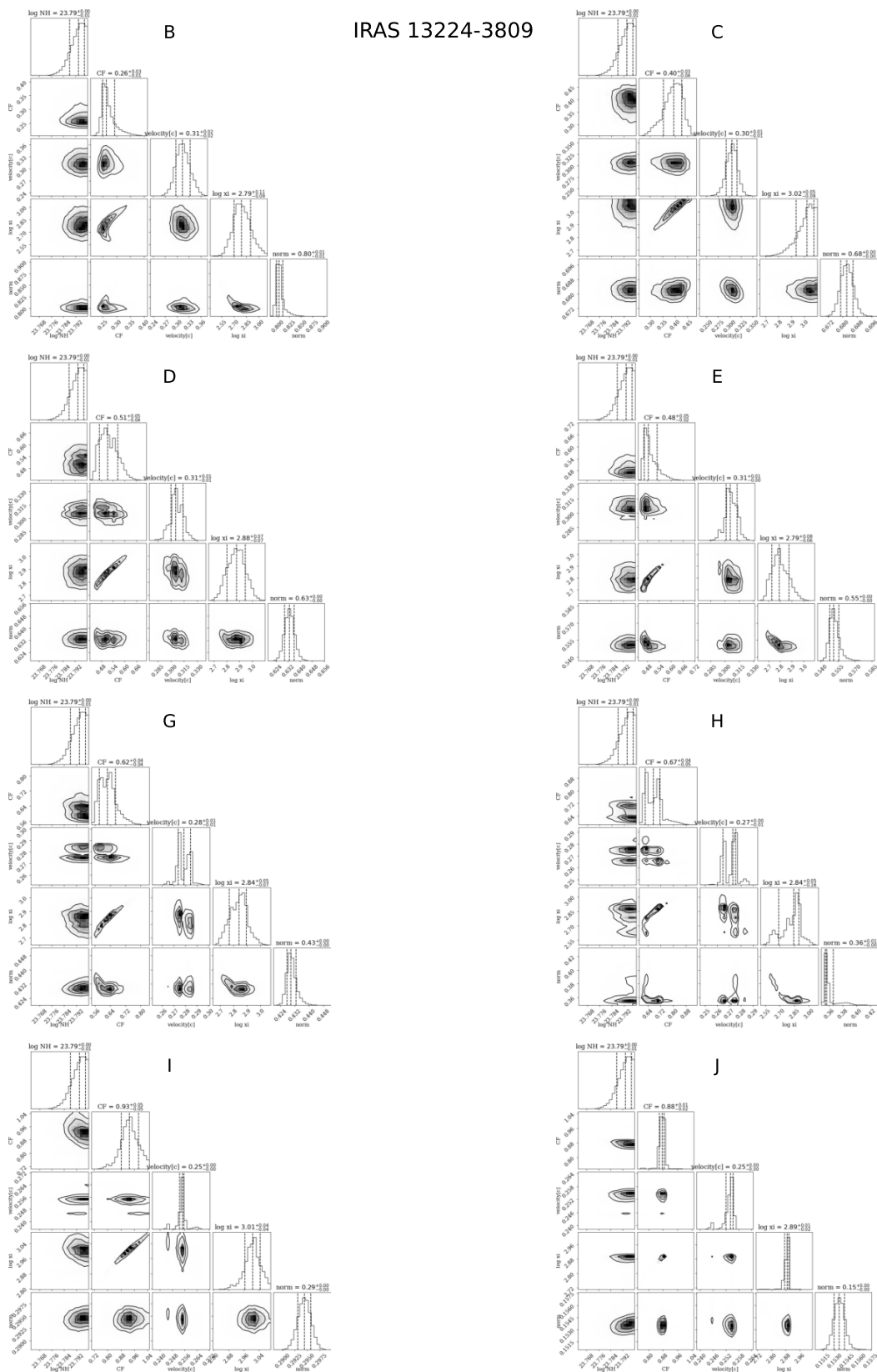


Figure A.2. Corner plots of the MCMC parameter estimation for all the spectral ratios except the spectral ratio F/A which is in the main text.

IRAS 13224-3809

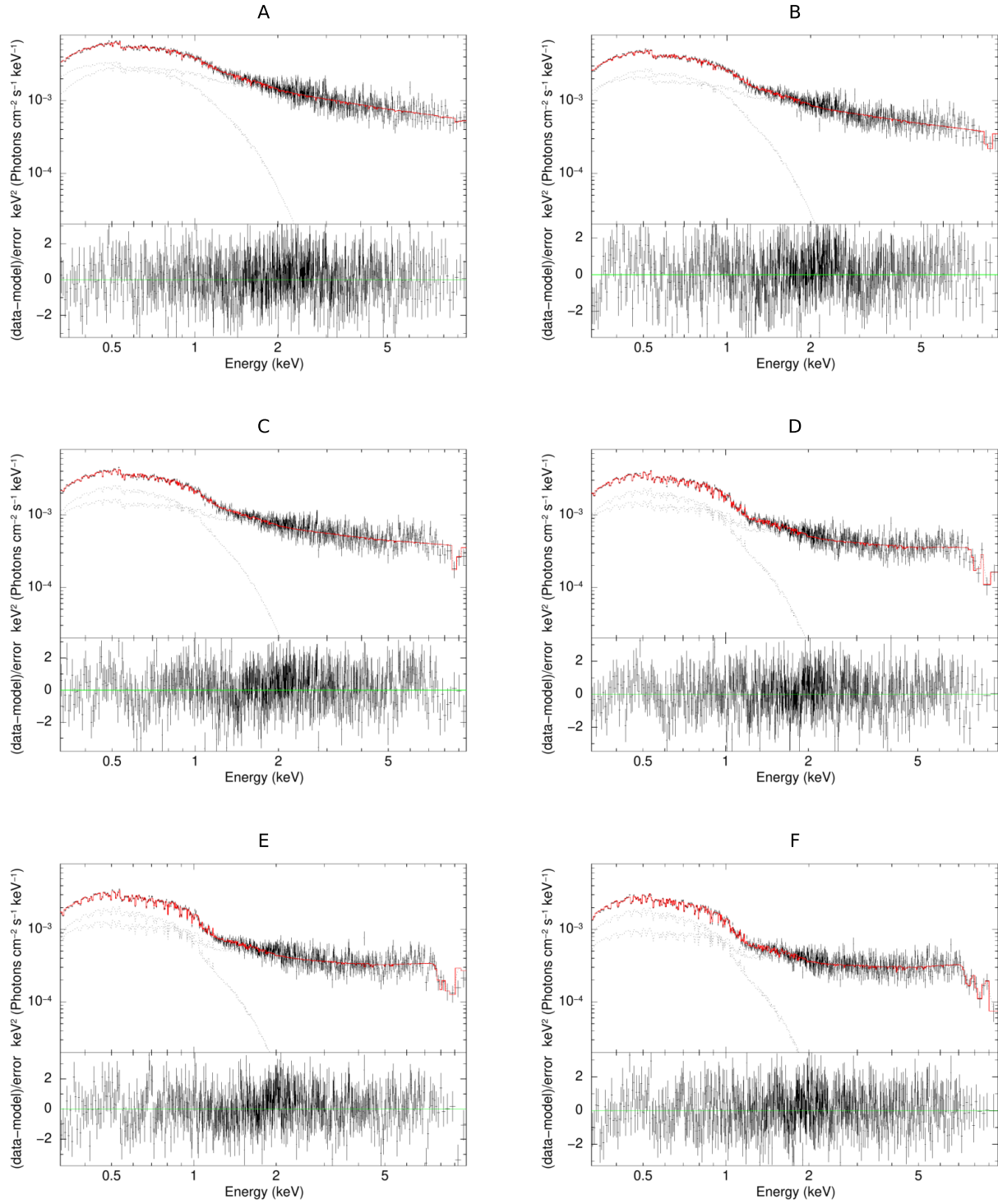


Figure A.3. Spectral fitting results of all the spectra except the spectrum F in the main text.

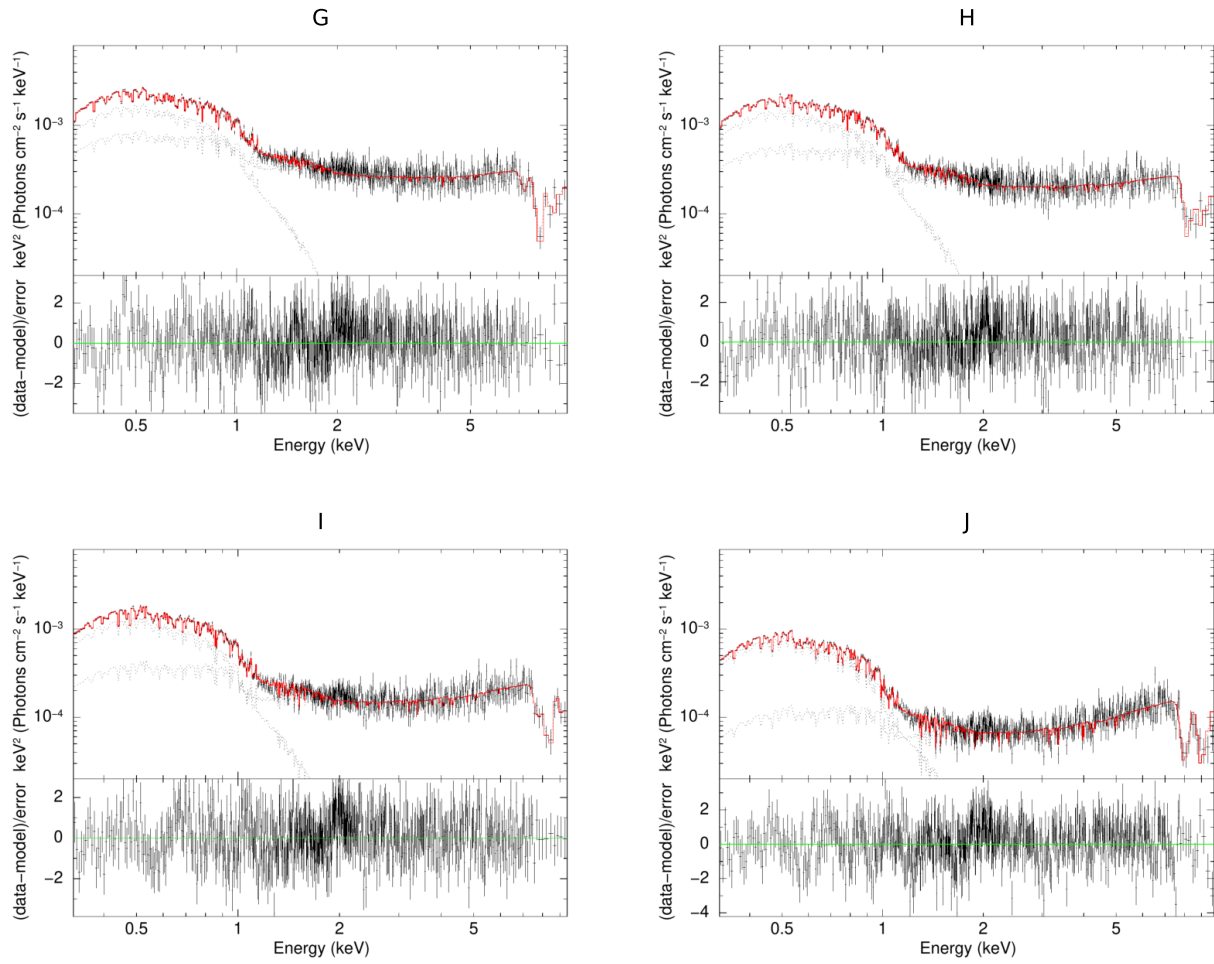


Figure A.4. (Cont.) Spectral fitting results of all the spectra except the spectrum F in the main text.